

Enabling Precise 2-D In-Plane Displacement Sensing With Low Latency for Motion Tracking Applications

Matthias Laimer¹, Thomas Kern¹, *Graduate Student Member, IEEE*, Lara Brukner¹,
Georg Schitter¹, *Senior Member, IEEE*, and Ernst Csencsics¹, *Member, IEEE*

Abstract—This article presents a sensor designed for real-time measurements of 2-D in-plane displacements. Utilizing laser speckle, the sensor comprises a high-speed camera and an field-programmable gate array (FPGA) to process data with low latency. Based on a 2-D cross-correlation algorithm implemented on the FPGA in the frequency domain, the sample in-plane displacement is measured. The camera captures images at rates of up to 8200 frames/s, with the FPGA processing the acquired images with a latency of 121 μ s for a region of interest (ROI) of 8×8 pixels. Experimental results demonstrate that the developed in-plane sensor effectively processes data in real-time, making it suitable for feedback control systems operating at frequencies up to several hundred hertz. The results also reveal a fundamental tradeoff between measurement range and frame rate/latency that can be exploited to match different application requirements.

Index Terms—High-speed imaging, in-plane motion sensing, real-time image processing.

I. INTRODUCTION

THE precise sensing and tracking of in-plane and out-of-plane motion is crucial for the success of modern high-tech manufacturing [1]. This is necessary to guarantee efficiency and quality in production, particularly in the automotive and semiconductor industries [2]. In this relation, achieving precise sample alignment during the manufacturing step is critical, whether for manipulation or quality inspection tasks [3], [4]. Primary sources that can misalign the sample during production are external disturbances, which can be either production or environmental-induced [5], [6]. Common causes of disturbances in production include vibrations from nearby machinery or the presence of people working close to the production area [7]. These disturbances typically occur at

frequencies up to several ten hertz and can result in motion blur, which degrades the overall quality of the production [6].

An effective strategy to mitigate these influences is to implement compensation-based production processes [8]. In this approach, the position of the sample is actively measured in six degrees of freedom (DOFs), and the production tool is adjusted through feedback control to maintain a constant relative position [9], [10]. However, to effectively suppress disturbances, the control bandwidth (BW) must be at least ten times greater than the frequency of the dominant disturbances, leading to control BWs of several hundred hertz. To ensure stable and robust control, sensors must be capable of measuring the sample position at least five times faster than the desired control BW [11]. This requires sensors with measurement rates of several kilohertz, and low latency on the order of hundreds of microseconds.

To measure the out-of-plane displacements on arbitrary surfaces with the required specifications, several principles are available [12]. Optical sensors used for this purpose include confocal chromatic methods, laser triangulation systems, and interferometric sensors [12], [13]. In addition to optical methods, also other noncontacting sensing principles such as capacitive and eddy-current sensors are used in various industrial applications [14], [15].

In contrast, measuring in-plane displacements with specifications similar to out-of-plane principles imposes several challenges [12]. One of the main difficulties is sensing lateral in-plane displacements on nonstructured technical surfaces [16]. A straightforward solution is to add structure to the sample, such as gratings or fiducial markers [17], [18]. In this way, a camera system can track the sample's displacement by implementing feature tracking or correlation-based algorithms [19]. However, it is often impractical or not possible to attach markers or targets for the application of sensing the sample displacements.

To address this limitation, coherent light sources, such as lasers, can be used to create laser speckle patterns to facilitate in-plane measurements without the need for prior sample preparation [20]. The requirement for obtaining these patterns is that the surface roughness needs to be on the scale of the optical wavelength, which is satisfied by most technical surfaces, including metals, plastics, and ceramics [20]. Laser speckle-based sensing can be categorized into interferometric and noninterferometric principles [21].

Received 20 February 2025; revised 20 August 2025; accepted 15 September 2025. Date of publication 29 September 2025; date of current version 15 October 2025. This work was supported in part by the Austrian Federal Ministry of Economy, Energy and Tourism; in part by the National Foundation for Research, Technology and Development; in part by the Christian Doppler Research Association; and in part by Micro-Epsilon Atensor GmbH and MICRO-EPSILON-MESSTECHNIK GmbH & Co. K.G. The Associate Editor coordinating the review process was Dr. Xianqiang Yang. (*Corresponding author: Matthias Laimer.*)

Matthias Laimer, Thomas Kern, Lara Brukner, and Ernst Csencsics are with the Christian Doppler Laboratory for Precision Measurements in Motion, Mechatronics and Power Electronics Institute (MPEI), Technische Universität Wien, 1040 Vienna, Austria (e-mail: laimer@acin.tuwien.ac.at).

Georg Schitter is with the Mechatronics and Power Electronics Institute (MPEI), Technische Universität Wien, 1040 Vienna, Austria.

Digital Object Identifier 10.1109/TIM.2025.3615282

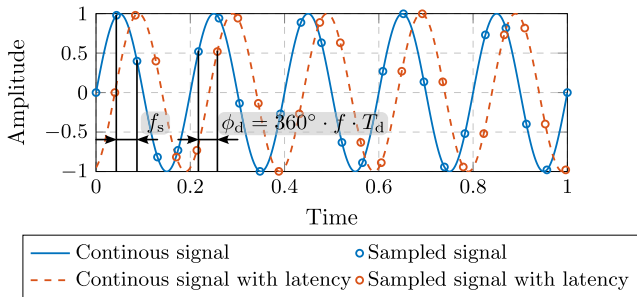


Fig. 1. Illustration of measurement rate and latency. The blue signal represents a harmonic signal with a frequency f , which is discretized by the sensor at the measurement rate f_s , indicated by blue dots. Considering sensor latency, the resulting orange signal is shifted by phase ϕ_d .

Interferometric methods, such as electronic speckle pattern interferometry, can achieve measurements with nanometer precision [22]. However, these techniques often require complex and bulky optical setups, making it challenging to integrate them into compact devices. They are mainly used under laboratory conditions for surface strain, stress, and deformation measurements [21], [22].

In contrast, noninterferometric sensors, which deploy the concept of objective laser speckle (OLSP), are particularly of interest for industrial applications because they do not require any additional optics aside from a coherent light source and a detector. This design enables highly integrated sensors and eliminates the negative effects of lens aberrations [23].

While both measurement methods can provide measurement rates of several kilohertz, the data processing still introduces a significant delay between the actual physical event and the point in time at which the measured information becomes available at the sensor output. Due to that, there are no sensors suitable for feedback-controlled in-plane motion tracking applications.

The contribution of this article is the development of a 2-D in-plane displacement sensor based on OLSPs, that achieves single-micrometer resolution with kHz BW and low latency. This advancement allows in-plane sensors to be effectively used in position feedback control, including precision motion tracking systems, with control BWs of up to several hundred hertz. The relevance of displacement sensing with low latency, as required for precision positioning systems, is introduced in Section II, followed by a description of in-plane displacement sensing using laser speckles in Section III. The in-plane sensor design and the experimental setup are introduced in Section IV. The performance of the 2-D in-plane sensor, regarding measurement range and latency, is evaluated in Section V. Finally, Section VI concludes this article.

II. RELEVANCE OF LATENCY

Measurement rate and latency are two important specifications that, along with other parameters (e.g., resolution, uncertainty, and repeatability), define the performance of time-discrete sensing systems [24], [25]. The measurement rate f_s of

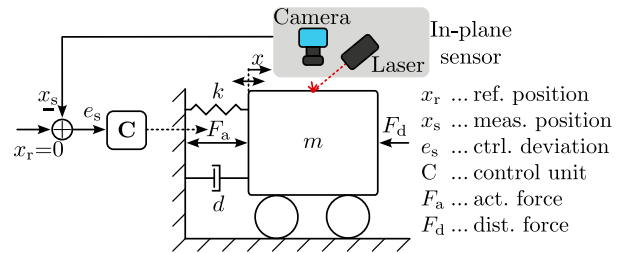


Fig. 2. Schematic illustration of a damped mass-spring. An in-plane sensor is used to precisely measure the position x of the mass m [11].

a sensor defines the maximum signal frequency $f_m \leq f_s/2$ that can be correctly measured according to the sampling theorem. Latency is the time between the occurrence of a physical event and the availability of the measurement result at the sensor's output. The latency of a sensor is thus a time delay T_d , leading, for example, to a phase shift ϕ_d between a harmonic input signal and the measured signal at the sensor output, as illustrated in Fig. 1. In a sensor system, various components, for example, analog-to-digital conversion, data processing, or internal dynamics are affecting the resulting latency and the overall delay budget [24].

For applications where a sensor is solely used for monitoring a system state, for example, for quality criteria, latency is not a critical factor since the time it takes until the measurement result becomes available at the sensor output is not relevant as long as it is reasonable stable [26]. However, for applications that require the control of a system state, the measurement rate and the latency have a significant impact on the performance [27]. For effectively controlling a system state, it is essential to not only measure data at a sufficient rate but also to process it within a specified time frame, defining the real-time capability of a system [28]. To ensure that the feedback control can react promptly to changes at the input and maintain stability, the latency of the sensor must stay within that specified time frame.

The simplified positioning system shown in Fig. 2, demonstrates the relevance of latency in feedback applications. A typical application of such a system is to maintain a moving mass, which can be a sample or a tool in a production process at a constant position $x_r = 0$. However, a disturbance force F_d , as outlined in Section I can cause misalignment. The mass position can be controlled in a closed-loop configuration by applying a force F_a , based on the measured in-plane position x_s , as illustrated by the conceptual sensor in Fig. 2. The damped mass-spring system is modeled by [5] and [29]

$$G_m(s) = \frac{x(s)}{F_a(s)} = \frac{1}{ms^2 + ds + k} \quad (1)$$

with m being the mass, d the damping, and k the spring constant. Exemplary, the system dynamics are illustrated in Fig. 3, for the parameters $k = 15.8$ kN/m, $d = 63$ Ns/m, and $m = 1$ kg.

To control the position x of the mass m , a PID controller in the form of

$$C_{\text{PID}}(s) = k_p + \frac{k_i}{s} + k_d s \quad (2)$$

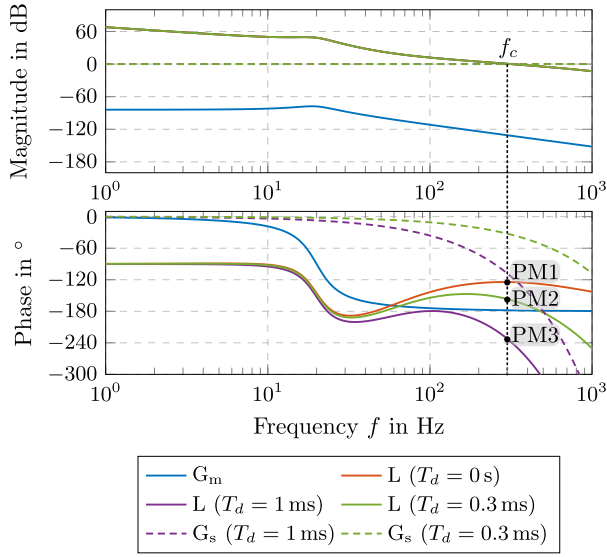


Fig. 3. Influence of sensor latency T_d on the closed-loop stability for a targeted cross-over frequency f_c . The bode plot shows the system dynamics G_m and equal loop gains with $f_c = 300$ Hz for all three latency scenarios. The phase margin for each scenario is shown in the phase response.

is designed for a cross-over frequency f_c of 300 Hz [30]. In this equation, k_p represents the proportional, k_i represents the integrator, and k_d represents the derivative gain. Such a high BW is required to sufficiently suppress disturbances as outlined in the introduction. For obtaining a stable closed-loop system, the phase margin (PM) of the loop gain $L = C_{PID}(s) \cdot G_m(s)$ serves as a stability criterion [31]. It is defined as the difference between the phase at the cross-over frequency f_c and -180° . The more the PM remains, the more stable and robust is the feedback-controlled system [30], [31], [32]. For demonstration, a PM of 50° at f_c is targeted in the control design. The loop-gain L without sensor latency ($T_d = 0$ s) is shown in Fig. 3.

To assess the impact of sensor latency on the achievable control BW, three scenarios are considered. In each scenario, the sensor operates at a measurement rate of $f_s = 1.5$ kHz, but with varying latencies of 0 s, 300 μ s, and 1 ms. The latency T_d of a sensor can be modeled as [33]

$$G_s(s) = e^{-T_d s}. \quad (3)$$

Consequently, the system dynamics can be expressed as

$$G(s) = \frac{1}{ms^2 + ds + k} e^{-T_d s}. \quad (4)$$

The resulting loop gains and phase responses with PM 1–3 at the cross-over frequency are illustrated in Fig 3. As the latency increases, the PM decreases. Even though the data are processed within 1 ms at the measurement rate of 1.5 kHz in the third case, a stable control design is not feasible, as the phase lag exceeds -180° at f_c . For a latency of $T_d = 300$ μ s, a phase margin of 30° remains, enabling reasonably stable feedback control for this and shorter latencies.

III. LASER SPECKLE AS SURFACE MARKER

When a coherent light source, such as a laser, is directed at an optically rough surface, the path lengths of the reflected

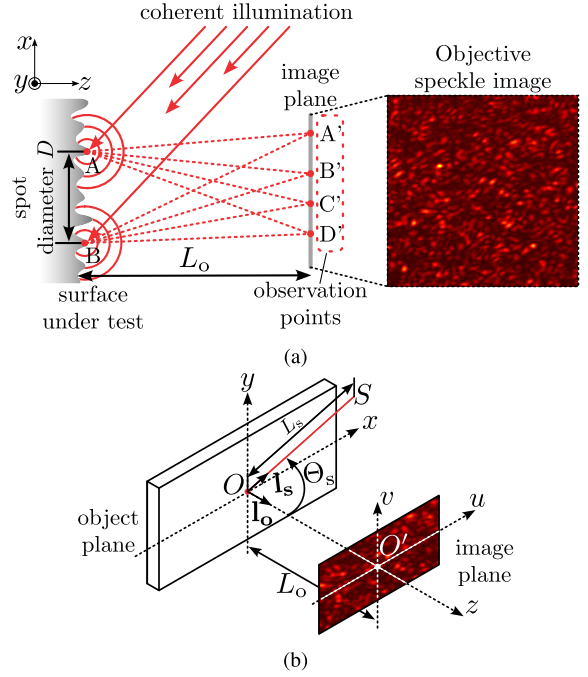


Fig. 4. Formation of an OLSP pattern in the image plane. (a) Coherent light source is directed onto an optically rough surface. Due to the surface roughness, the light path length varies, which leads to constructive or destructive interference on the detector. (b) Sensor alignment for measuring in-plane displacement in the object plane.

light will vary [20]. This variation leads to phase differences due to the surface structure, as illustrated in Fig. 4(a). If a detector is positioned at a distance L_o from the sample, the reflected light rays will interfere either constructively or destructively at the individual pixels. In the case of free-space propagation [see Fig. 4(a)], the reflection at each surface point (e.g., A) contributes to each detector point A' to D'. Considering this effect across all pixels of a sensor array, an OLSP pattern is formed.

The movement of the speckle pattern in the image plane due to an in-plane displacement of the object can be analytically derived [23]. In Fig. 4(b), a source S is placed at a distance L_s from the origin O of the object plane illuminating the optically rough surface. The direction of S is denoted by the vector $\mathbf{l}_s = [l_{sx}, l_{sy}, l_{sz}]^T$. The image plane with its origin O' is positioned at a distance L_o from the object plane, which is oriented according to the vector $\mathbf{l}_o = [l_x, l_y, l_z]^T$.

For the general case, speckle pattern shifts in the image plane caused by translational in-plane displacements, object rotations, and stress can be described as

$$\begin{aligned} A_u = & -a_x \left(\frac{L_o}{L_s} (l_{sx}^2 - 1) + l_x^2 - 1 \right) - a_y \left(\frac{L_o}{L_s} l_{sx} l_{sy} + l_x l_y \right) \\ & - a_z \left(\frac{L_o}{L_s} l_{sx} l_{sz} + l_x l_z \right) - L_o (\epsilon_{xx} (l_{sx} + l_x) \\ & + \epsilon_{xy} (l_{sy} + l_y) + \Omega_z (l_{sy} + l_y) - \Omega_y (l_{sz} + l_z)) \end{aligned} \quad (5)$$

and

$$A_v = -a_x \left(\frac{L_o}{L_s} l_{sy} l_{sx} + l_y l_x \right) - a_y \left(\frac{L_o}{L_s} (l_{sy}^2 - 1) + l_y^2 - 1 \right)$$

$$\begin{aligned}
& -a_z \left(\frac{L_0}{L_s} l_{xy} l_{sz} + l_y l_z \right) - L_0 (\epsilon_{yy} (l_{xy} + l_y) \\
& + \epsilon_{xy} (l_{sx} + l_x) - \Omega_z (l_{sx} + l_x) - \Omega_x (l_{sz} + l_z)) \quad (6)
\end{aligned}$$

with $\mathbf{a} = [a_x, a_y, a_z]^T$ being the translation and with $\boldsymbol{\Omega} = [\Omega_x, \Omega_y, \Omega_z]^T$ being the rotation vector of the object, respectively. To minimize crosstalk between the in-plane motion directions, the sensor is aligned as illustrated in Fig. 4(b), with $\mathbf{l}_0 = [0, 0, 1]^T$ and $\mathbf{l}_s = [0, \sin(\theta_s), \cos(\theta_s)]^T$. Disregarding stress, described by ϵ_{xx} , ϵ_{xy} and ϵ_{yy} , rotations and translational out-of-plane motions, and assuming a perfectly collimated light source S , (radius of curvature L_s becomes infinite) [34], this results in the simplified equations

$$A_u = a_x \quad (7)$$

and

$$A_v = a_y. \quad (8)$$

There an in-plane displacement in the object plane is directly translated to an equal shift of the speckle pattern in the image plane.

IV. IN-PLANE SENSOR SYSTEM DESIGN

For the application in precise, feedback-controlled motion tracking tasks, a sensor with a BW of at least 1 kHz and a latency of less than 300 μ s is required, as outlined in Section II. To measure only in-plane displacements (see Section III), the sensor must be positioned parallel to the sample surface. For an optimal operation, the mean speckle diameter needs to be at least three to five times the pixel size of the detector, which can be adjusted by the working distance L_0 and the spot diameter of the light source [35]. To meet the targeted specifications, the in-plane sensor comprises a dedicated high-speed camera, real-time capable hardware for rapid image acquisition and processing, and a collimated coherent light source.

A. High-Speed Imaging and Acquisition

The MIRA 050 (ams-OSRAM AG, Premstaetten, Austria) is a pipelined global shutter CMOS camera with a resolution of 600 (H) \times 800 (V) and a pixel size of 2.79 μ m. A pipelined global shutter means, that the exposure of an image $n+1$ can already happen during the readout of the previous image n , as illustrated in Fig. 5(a). The camera implements the MIPI CSI-2 interface, consisting of a high-speed clock and single data line pair for the image transmission at a rate of 1.26 Gb/s. The camera is configured via an I2C interface. At full resolution and 10 bit analog-to-digital converter (ADC) mode, a framerate of 205 fps is achieved. By decreasing the camera region of interest (ROI), the framerate can be increased, leading to a maximum framerate of 9000 fps at a resolution of 400 \times 1 pixel.

For image acquisition and processing, the AVNET ULTRA 96 V2 (Avnet, Inc., Phoenix, Arizona, USA) development board is used. It implements an AMD Zynq UltraScale+ field-programmable gate array (FPGA) chip and a Quad-core ARM Cortex-A53 processing unit. The MIPI CSI-2 RX intellectual property (IP) provided by Xilinx (AMD Inc., Santa Clara, CA,

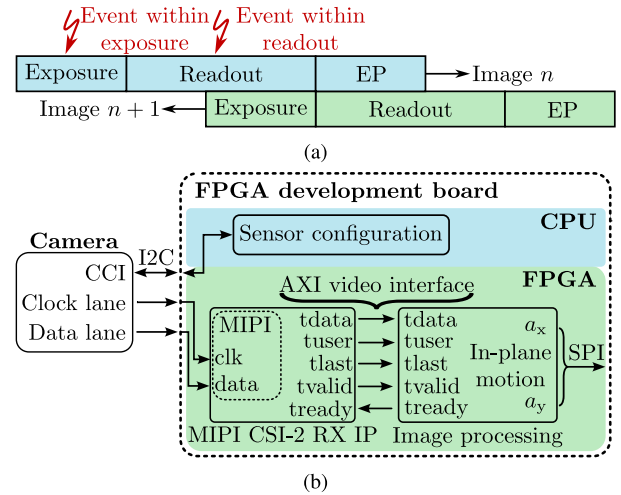


Fig. 5. Acquisition and processing of the acquired images. (a) In-plane sensor has three internal states: *exposure*, *readout*, and *EP*. The latency of the sensor varies depending on when an event occurs within the processing chain. (b) Image acquisition and processing block diagram shows the camera configuration being handled by the CPU, while high-speed in-plane displacement calculations are carried out on the FPGA.

TABLE I
DESCRIPTION OF THE AXI VIDEO INTERFACE SIGNALS

AXI video signal	Description	Type
tdata	Pixel data	Output
tuser	Start of frame (first pixel of a new image)	Output
tlast	End of line (last pixel of a transmitted row)	Output
tvalid	Signalizes valid pixel data	Output
tready	Subsystem is ready to receive pixel data	Input

USA) enables the acquisition of the transmitted images at a data rate of 1.26 Gb/s. The received pixels are transmitted to the image processing block [see Fig. 5(b)], via the AXI video interface. A description of the AXI video interface signals is given in Table I. The AXI video clock for all subsystems on the FPGA is 300 MHz.

B. Low-Latency Data Processing

As outlined in Section III, any in-plane displacement a_x and a_y occurring in the object plane results in a corresponding shift

$$u'_i = u_i + a_x \quad (9)$$

and

$$v'_i = v_i + a_y \quad (10)$$

of the speckle pattern in the image plane. In these equations, u_i and v_i correspond to the pixel coordinates before translation. To extract the unknown sample displacements a_x and a_y from the captured speckle images, several algorithms are available, which can be categorized into feature-based and correlation-based [19]. To achieve robust and fast in-plane displacement sensing, the 2-D cross-correlation algorithm

$$C_{cc} = \sum_{i=-N}^N \sum_{j=-N}^N I_1(u_i, v_j) I_n(u'_i, v'_j) \quad (11)$$

with $I_1(u_i, v_j)$ being the reference and $I_n(u'_i, v'_j)$ a subsequently captured image, is selected.

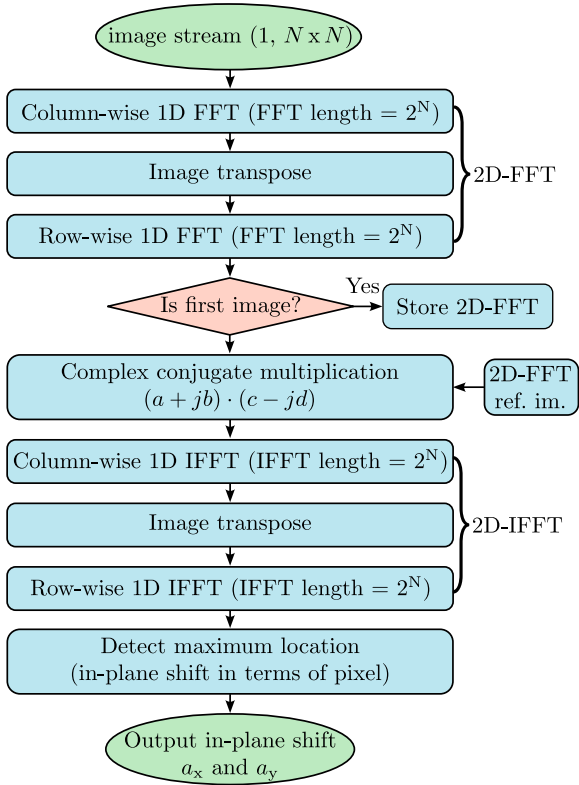


Fig. 6. Flowchart of the 2-D cross-correlation algorithm implemented on the FPGA.

The image size is $N \times N$, with $N > 0$. In the resulting cross-correlation map C_{cc} , an in-plane shift is detected as a peak, which is highest if the two images are correlated. This is valid until the in-plane displacement exceeds a certain translation, which is about half the image dimension $N/2$. Due to speckle decorrelation, the peak height gradually decreases for larger displacement until it falls below the noise floor and can no longer be detected [34]. In the case of the designed in-plane sensor, the location of the peak in the cross-correlation map corresponds directly to the sample in-plane shift a_x and a_y .

To efficiently implement the 2-D cross-correlation algorithm on the FPGA, the calculation of C_{cc} is performed in the frequency domain rather than the spatial domain. This leads to

$$C_{cc} = \mathcal{F}^{-1}\{\mathcal{F}\{I_1(u, v)\}\mathcal{F}^*\{I_n(u', v')\}\} \quad (12)$$

where \mathcal{F} corresponds to the Fourier transformation [19]. This approach has the advantage of reducing the costly iteration over both image coordinates to a multiplication of the Fourier-transformed images. The flowchart of the algorithm implemented on the FPGA is illustrated in Fig. 6. The image captured by the camera is transmitted as a stream of $N \times N$ pixels, with pixel data read out column-wise. To calculate the Fourier transform of the images, the 1-D fast Fourier transformation (FFT) IP provided by Xilinx is utilized. The FFT length is chosen to be a power of two. Since a 2-D FFT of the images is required, the process starts with calculating the FFT over all image columns, followed by transposing the image data and applying the FFT on the rows of the image. The 2-D Fourier transform of the reference image is stored in

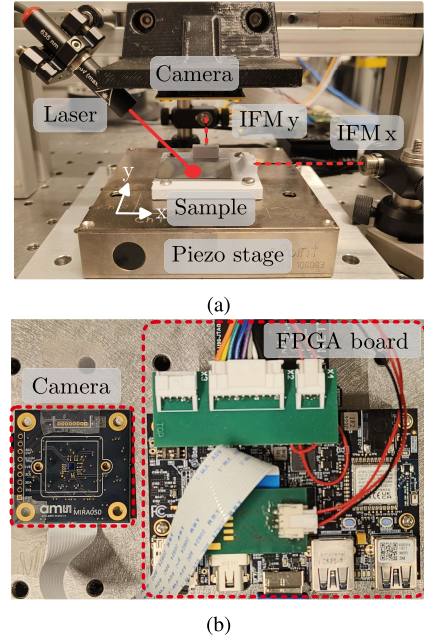


Fig. 7. Experimental setup of the 2-D in-plane sensor. (a) Sensor comprises a laser, a camera, and an FPGA. An optically rough sample is mounted on a two-axis piezo stage. Interferometers IFM x and IFM y serve as References. (b) Acquired images are sent to the FPGA for real-time calculation of the sample in-plane displacements.

the RAM of the FPGA, as it is required for the multiplication with the complex conjugate of every subsequent image.

Finally, a 2-D inverse FFT is applied following the same scheme. A maximum search in the resulting cross-correlation map C_{cc} to find the location of the peak is done in the last step to retrieve the measured in-plane displacements a_x and a_y . The image processing begins directly with the first pixel received and is fully pipelined and parallelized.

C. Experimental Setup

For evaluating the performance of the developed 2-D in-plane sensor, an experimental setup is designed as illustrated in Fig. 7(a). An optically rough aluminum sample is mounted on the mover of a two-axis piezo stage NPXY100-100 (Motion Solutions, Irvine, CA, USA), with a maximum actuation range of $\pm 50 \mu\text{m}$ (closed-loop), and a resolution of 5 nm rms . Furthermore, two interferometers IDS3010 (Attocube AG, Haar, Germany) with a resolution of 1 nm rms and a BW of 100 kHz are used for reference measurements of the sample position. For the in-plane sensor, a collimated laser diode PL204 (Thorlabs, Newton, NJ, USA) with a wavelength of 635 nm and an output power of 1 mW is used. It is directed onto the rough surface at an incident angle of $\theta_s = 45^\circ$. The light is diffusely reflected to the in-plane sensor [see Fig. 7(b)], consisting of the high-speed CMOS camera MIRA 050 and an FPGA development board AVNET ULTRA 96 V2 for data processing in real-time. The camera is placed at a distance $L_0 = 40 \text{ mm}$ to the sample, leading to a mean speckle diameter of $10 \mu\text{m}$. The sensor data of the interferometer, the internal capacitive sensors, and the developed speckle

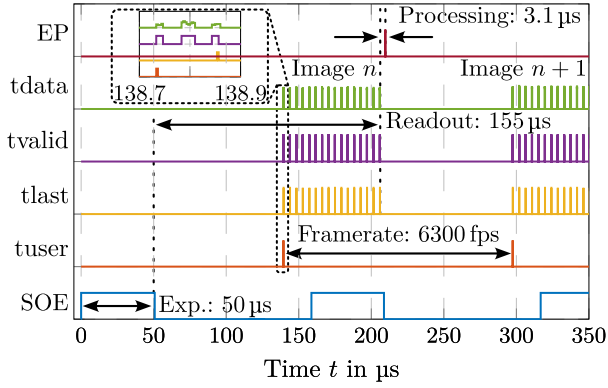


Fig. 8. Detailed timing analysis shown for the ROI 16 with a frame rate of 6300 fps. The readout of all pixels takes $155 \mu\text{s}$. After the last pixel is received, it takes another $3.1 \mu\text{s}$, until the in-plane displacement is calculated.

TABLE II
IN-PLANE SENSOR TIMINGS FOR DIFFERENT ROIS

ROI	Frame rate	Readout	EOP	Latency min.	Latency max.
64	2700 fps	369 μs	27.3 μs	396.3 μs	765.3 μs
32	4545 fps	226 μs	9.1 μs	235.1 μs	461.7 μs
16	6300 fps	155 μs	3.1 μs	158.1 μs	313.6 μs
8	8200 fps	120 μs	1.4 μs	121.4 μs	240.9 μs

sensor are acquired by a MicroLabBox (dSPACE, Paderborn, Germany), operating at a sampling frequency of 60 kHz.

D. Timing and Latency Evaluation

As discussed before, precise knowledge of the sensor latency is essential for many applications. Consequently, it is important to consider the latency budget at each processing step of the sensor pipeline, as shown in Fig. 5(a). Table II summarizes the sensor timings for different camera ROIs. For example, ROI 64 indicates that a 64×64 -pixel area at the camera center is read out. Since the processing of acquired images on the FPGA starts with the first pixel received, the sensor state end of processing (EP) determines the duration of data processing from the last pixel received until the in-plane displacement becomes available at the sensor output. The state *readout* defines the duration between the end of exposure and the last pixel received for a specific ROI. A precise illustration of the sensor timings for ROI 16 is shown in Fig. 8. It illustrates the three sensor states previously discussed for an image n . The time between the falling edge of the exposure and the first pixels arrived, indicated by the tuser flag, at the FPGA, includes both the global shutter time of the camera and the analog-to-digital conversion of the pixels.

Since the designed sensor operates time discrete, the latency is dependent on when an event occurs in relation to the current sensor state, as illustrated in Fig. 5(a). If the event occurs during the exposure of image n , the in-plane displacement will be detected at the end of EP for image n . However, if the event occurs right after the exposure of image n , within the *readout* state, the in-plane displacement is detected after processing image $n+1$, leading to an increased latency. Due to this the sensor latency will vary between $T_{d,\min} = t_{\text{readout}} + t_{\text{ep}}$ and $T_{d,\max} = 2 \cdot t_{\text{readout}} + t_{\text{ep}}$, with t_{readout} being the *readout* and

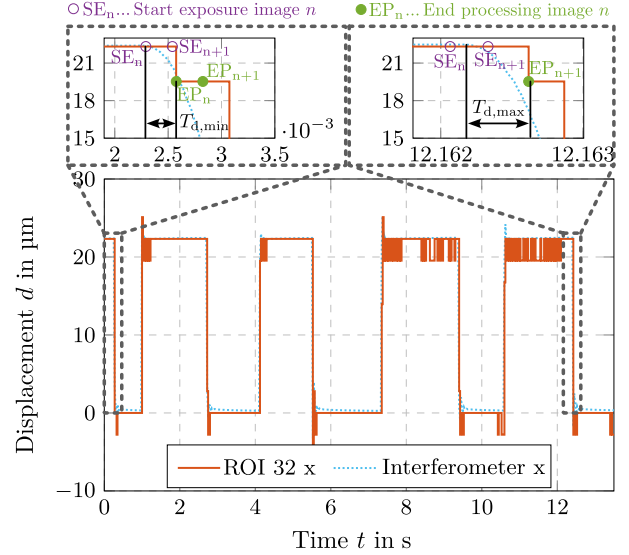


Fig. 9. Relation between event occurrence and latency. In the top left image, the step is applied during the camera's exposure, resulting in minimal latency for the sensor. Conversely, in the top right image, the step is applied shortly after the exposure, leading to a maximal latency in the sensor's response.

t_{ep} the EP time, respectively. Since the exposure of image $n+1$ can already start within the readout of image n , the exposure time does not affect the sensor latency as long as $t_{\text{exp}} \leq t_{\text{readout}}$.

To experimentally demonstrate the varying sensor latency, $k = 1000$ steps with a step height of $21 \mu\text{m}$ are applied at random time stamps to the piezo stage, as shown in Fig. 9 for the ROI 32 along the motion direction x . In this evaluation, the piezo stage operates in an open-loop configuration, leading to slightly varying step heights. The interferometer reading serves as the ground truth for this experiment. To identify the sensor latencies, the gradient of the interferometer and speckle sensor signals are calculated. This allows to quantify at which point each sensor detects the applied steps. Threshold of $\delta x_{\text{IFM}} = 6 \mu\text{m/s}$ and $\delta x_s = 20 \mu\text{m/s}$ for the interferometer and speckle sensor are chosen, respectively. These values are selected slightly above the noise level of the gradient signals, to minimize faulty step detections. The time difference at which the interferometer and the speckle sensor signals exceed their individual thresholds determines the latency of the speckle sensor. The latency of the interferometer is considered negligible as it operates at a measurement rate that is more than ten times higher than that of the speckle sensor.

The minimal and maximal latency of $T_{d,\min} = 235 \mu\text{s}$ and $T_{d,\max} = 466 \mu\text{s}$ (as shown in the top left and top right plots of Fig. 9) are recorded. These latencies align well with the expected sensor latencies for this ROI (see Table II). The observed deviations can be attributed to the sampling time of the data acquisition system, which operates at a rate of 60 kHz corresponding to a sampling time of $16.67 \mu\text{s}$.

V. EXPERIMENTAL RESULTS

The developed 2-D in-plane sensor performance is characterized based on its measurement range and dynamic response for the defined ROIs, shown in Table II. To evaluate the sensor's measurement range, a linear trajectory from $-50 \mu\text{m}$

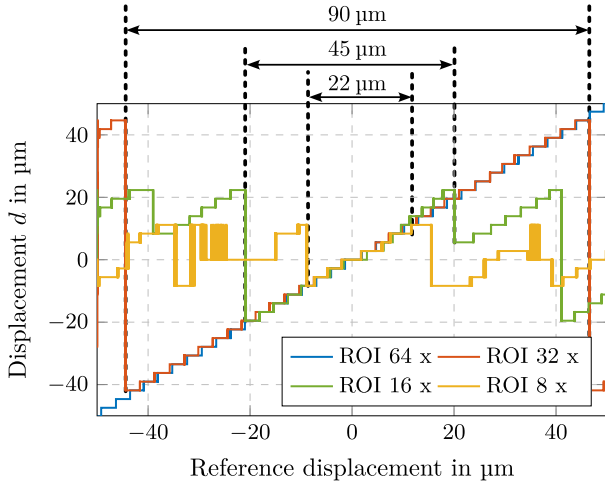


Fig. 10. Measurement ranges of the in-plane sensor in x-direction for different ROIs.

to $50 \mu\text{m}$ is applied to the piezo stage along motion direction x . For this evaluation, the piezo stage is operated in closed-loop, and the interferometer is taken as reference.

The achievable measurement range for different ROIs are illustrated in Fig. 10. It can be seen that the measurement range corresponds to the selected ROI times the pixel size. With the exception of ROI 64, the actuation range of the piezo stage is not sufficient to travel the entire measurement range. However, based on the evaluated ranges, the range for ROI 64 can be extrapolated to be $180 \mu\text{m}$. If the piezo stage exceeds the range of a specific sensor configuration (see Fig. 10), displacement sensing is no longer possible, due to speckle decorrelation. Since the camera pixel size is $2.79 \mu\text{m}$, the sample position can only be measured in discrete steps, as can be seen in Fig. 10. The pixel size, therefore, defines the resolution of the developed in-plane sensor. This introduces an experimentally evaluated quantization error of half the pixel size of $\pm 1.395 \mu\text{m}$, which is noticeable in Fig. 9.

The long-term stability regarding thermal drift has been assessed using the experimental data utilized for the timing and latency analysis in Section IV-D, with a portion of this data depicted in Fig. 9. However, given the sensor's resolution of $2.79 \mu\text{m}$, no significant effect of thermal drift on the in-plane measurements is observed. Another potential source of error arises from environmental influences such as air turbulence, which can introduce refractive index fluctuations and alter the speckle pattern. However, at the relatively short stand-off distance of 40 mm , such effects are only expected to become significant in the sub-micrometer regime and are therefore negligible for the present sensor resolution of $2.79 \mu\text{m}$ [36]. In addition, out-of-plane motion can influence in-plane measurements and contribute to speckle decorrelation. However, for the developed sensor, which is intended for high-BW, low-latency motion tracking within displacement ranges of several tens of micrometers, the effect of axial displacement is considered negligible as long as systems without high magnification are employed, which applies to the present design [37].

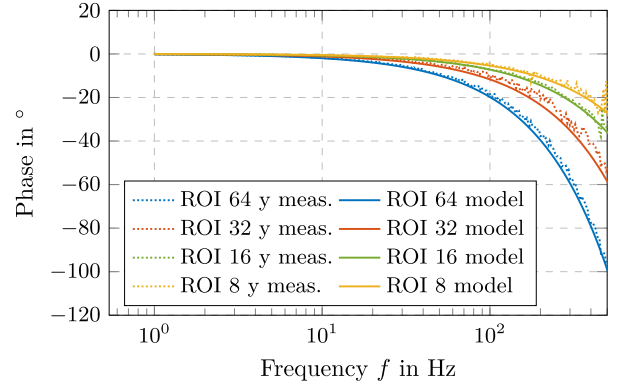


Fig. 11. Verification of the in-plane sensor dynamics for various ROIs, compared to the modeled sensor latencies. As a reference, the interferometer measurements are used.

TABLE III
EXPERIMENTAL PERFORMANCE EVALUATION FOR DIFFERENT ROIS

	ROI 64	ROI 32	ROI 16	ROI 8
Range	180 μm	90 μm	45 μm	22 μm
effective latency $\overline{T_d}$	580.8 μs	348.4 μs	235.9 μs	181.2 μs
Phase(@ 100 Hz)	20°	10°	7°	5°
Phase(@ 200 Hz)	38°	21°	14°	10°
Phase(@ 300 Hz)	57°	31°	20°	15°
Phase(@ 400 Hz)	77°	42°	27°	20°

To further improve the sensor resolution, interpolation and curve fitting, such as higher order polynomial functions, can be implemented. However, considering the aspect of processing the acquired data with low latency and that such algorithms are costly to implement in hardware, it poses a trade-off in terms of achievable resolution and latency [38]. As FPGAs have limited hardware resources, and since the 2-D cross-correlation calculation already occupies most of these resources, additional algorithms aimed to enhance the sensor resolution are not considered. As the sensor system is symmetric, the same measurement range for the motion direction y is achieved (data not shown).

The dynamics of the sensor are identified by applying a sine sweep to the y -axis of the piezo stage, over a frequency range from 1 to 500 Hz with an amplitude of $15 \mu\text{m}$. The piezo stage is driven in open-loop to ensure that control dynamics do not influence the experiment. The interferometer is again taken as reference. Since the dynamics are identified based on a sequence of harmonic signals, it is expected that the effective latency of the sensor is

$$\overline{T_d} = \frac{T_{d,\min} + T_{d,\max}}{2} \quad (13)$$

for feedback control applications. Fig. 11 illustrates the performed dynamics evaluation for the defined ROIs. Since sensor latency [see (3)] does not affect the gain of the system, only the phase response of the in-plane sensor is illustrated. The dashed lines show the measured phase response, whereas the solid lines are the modeled effective latencies $\overline{T_d}$, which are in good agreement with the measured latencies. The sensor phase for the defined ROIs with the corresponding measurement ranges

TABLE IV

COMPARISON OF THIS WORK WITH STATE-OF-THE-ART IN-PLANE DISPLACEMENT SENSORS. REPORTED SPECIFICATIONS INCLUDE BW, LATENCY (LAT.), RESOLUTION (RES.), MEASUREMENT RANGE (RANGE), AND SURFACE COMPATIBILITY (SURF.). HERE, N.A. = NOT AVAILABLE

Method	BW	Lat.	Res.	Range	Surf.
This work	8.2 kHz	121 μ s	2.79 μ m	22 μ m	diffuse
Charrett et al. [41]	0.5 kHz	n.a.	<1 μ m	1.2 mm	diffuse
Csencsics et al. [8]	10 Hz	n.a.	3 μ m	300 μ m	diffuse
Ge et al. [42]	20 Hz	n.a.	10 μ m	n.a.	diffuse

and effective latencies at various frequencies are summarized in Table III. As expected, a larger ROI leads to an increased measurement range at the cost of a higher mean latency \bar{T}_d . On the other hand, using a reduced ROI increases the applicability of the sensor for high-BW applications, as motivated in Section II. Considering sample motion tracking applications, a measurement range of several tens of micrometers may anyhow be sufficient. Revisiting the initial requirement of a cross-over frequency of 300 Hz, the sensor configurations up to ROI 32 can be used, leading to remaining PMs of 20°, 30°, and 35°, respectively.

In summary, the experimental evaluation proves that the proposed sensor can measure in-plane displacements with a resolution of 2.79 μ m in two with a measurement rate of 8200 fps and a low effective latency of 182 μ s, which makes it well suited for position feedback control applications.

VI. CONCLUSION AND OUTLOOK

This article presents the development of a sensor designed to measure 2-D in-plane displacements with low latency, sampling rates of several kilohertz, and single-micrometer resolution. OLSP patterns, obtained by directing a coherent light source onto an optically rough surface, are used as markers for in-plane displacement sensing. The developed laser speckle-based in-plane sensor comprises solely a low-cost, high-speed camera without optical components and an FPGA for real-time data processing, which enables a compact and robust sensor design. To extract in-plane surface displacements from the captured images, a 2-D cross-correlation algorithm solved in the frequency domain is implemented in hardware on the FPGA. This allows in-plane displacement sensing at rates up to 8200 fps with a low latency of only 182 μ s for a ROI of 8 \times 8 pixels over a range of 22 μ m. With a pixel size of 2.79 μ m, the sensor achieves a resolution on the single micrometer scale. While state-of-the-art approaches have demonstrated resolutions of 0.1 pixel, they typically rely on computationally intensive postprocessing on external computers, limiting real-time performance by introducing latencies of several milliseconds [8], [19], [39]. To put these limitations into perspective, Table IV provides a comparison with research-grade displacement sensors, highlighting the trade-offs in BW, latency, resolution, measurement range, and surface compatibility. In contrast, the proposed approach achieves significantly higher speeds of several thousand frames per second and latencies of only a few hundred microseconds. Experimental evaluations demonstrate that real-time in-plane motion sensing of nonstructured surfaces is enabled, which

allows the sensor to be used for sample motion tracking applications that require feedback control BWs of several hundred hertz.

Building on these capabilities, future work will focus on integrating the sensor into real-world scenarios, such as robotic sample tracking [40]. In this context, particular attention will be given to challenges, including the coordination of multiple sensors, reliable tracking under full six DOF (6-DOF) motion, and precise calibration of the sensor within the robot's coordinate frame.

VII. ACKNOWLEDGMENT

The authors acknowledge TU Wien Bibliothek for financial support through its Open Access Funding Programme.

REFERENCES

- [1] D. Imkamp et al., "Herausforderungen und trends in der fertigungsmesstechnik—Industrie 4.0," *TM-Technisches Messen*, vol. 83, nos. 7–8, pp. 417–429, Jul. 2016.
- [2] H. Lasi, P. Fettke, H.-G. Kemper, T. Feld, and M. Hoffmann, "Industry 4.0," *Bus. Inf. Syst. Eng.*, vol. 6, no. 4, pp. 239–242, 2014.
- [3] M. F. Heertjes et al., "Control of wafer scanners: Methods and developments," in *Proc. Amer. Control Conf. (ACC)*, Jul. 2020, pp. 3686–3703.
- [4] S. Mishra, J. Coaplen, and M. Tomizuka, "Precision positioning of wafer scanners segmented iterative learning control for nonrepetitive disturbances [applications of control]," *IEEE Control Syst. Mag.*, vol. 27, no. 4, pp. 20–25, Apr. 2007.
- [5] D. Wertjanz, E. Csencsics, and G. Schitter, "Three-DoF vibration compensation platform for robot-based precision inline measurements on free-form surfaces," *IEEE Trans. Ind. Electron.*, vol. 69, no. 1, pp. 613–621, Jan. 2022.
- [6] C. G. Gordon, "Generic criteria for vibration-sensitive equipment," *Proc. SPIE*, vol. 1619, pp. 71–85, Feb. 1992.
- [7] R. K. Mobley, *Vibration Fundamentals*. Boston, MA, USA: Butterworth-Heinemann, 1999.
- [8] E. Csencsics, "Integrated compensation-based laser sensor system for in-plane and out-of-plane target tracking," *Appl. Opt.*, vol. 59, no. 20, pp. 6138–6147, Jul. 2020.
- [9] E. Csencsics, M. Thier, S. Ito, and G. Schitter, "Supplemental peak filters for advanced disturbance rejection on a high precision endeffector for robot-based inline metrology," *IEEE/ASME Trans. Mechatronics*, vol. 27, no. 4, pp. 2258–2266, Aug. 2022.
- [10] D. Wertjanz, T. Kern, A. Pechhacker, E. Csencsics, and G. Schitter, "Robotic precision 3D measurements in vibration-prone environments enabled by active six DoF sample-tracking," in *Proc. IEEE/ASME Int. Conf. Adv. Intell. Mechatronics (AIM)*, Jul. 2022, pp. 1441–1446.
- [11] R. M. Schmidt, G. Schitter, A. Rankers, and J. van Ejjik, *The Design of High Performance Mechatronics: High-Tech Functionality By Multi-disciplinary System Integration*, 2nd ed., Delft, The Netherlands: Delft Univ. Press, 2014.
- [12] J. G. Webster, *The Measurement, Instrumentation, and Sensors Handbook*. Boca Raton, FL, USA: CRC Press, 1999.
- [13] X. Diao, P. Hu, Z. Xue, and Y. Kang, "High-speed high-resolution heterodyne interferometer using a laser with low beat frequency," *Appl. Opt.*, vol. 55, no. 1, pp. 110–116, Jan. 2016.
- [14] Y. Ye, C. Zhang, C. He, X. Wang, J. Huang, and J. Deng, "A review on applications of capacitive displacement sensing for capacitive proximity sensor," *IEEE Access*, vol. 8, pp. 45325–45342, 2020.
- [15] M. R. Nabavi and S. N. Nihtianov, "Design strategies for eddy-current displacement sensor systems: Review and recommendations," *IEEE Sensors J.*, vol. 12, no. 12, pp. 3346–3355, Dec. 2012.
- [16] P. K. Rastogi, *Trends in Optical Nondestructive Testing and Inspection*, 2nd ed., Amsterdam, The Netherlands: Elsevier, 2003.
- [17] A. N. André, P. Sandoz, B. Mauzé, M. Jacquot, and G. J. Laurent, "Sensing one nanometer over ten centimeters: A microencoded target for visual in-plane position measurement," *IEEE/ASME Trans. Mechatronics*, vol. 25, no. 3, pp. 1193–1201, Jun. 2020.
- [18] M. Grédiac, B. Blaysat, and F. Sur, "Extracting displacement and strain fields from checkerboard images with the localized spectrum analysis," *Experim. Mech.*, vol. 59, no. 2, pp. 207–218, Feb. 2019.

- [19] B. Pan, K. Qian, H. Xie, and A. Asundi, "Two-dimensional digital image correlation for in-plane displacement and strain measurement: A review," *Meas. Sci. Technol.*, vol. 20, no. 6, Apr. 2009, Art. no. 062001.
- [20] J. W. Goodman, "Some fundamental properties of speckle*," *J. Opt. Soc. Am.*, vol. 66, no. 11, p. 1145, Nov. 1976.
- [21] I. M. De la Torre, M. D. S. Hernández Montes, J. M. Flores-Moreno, and F. M. Santoyo, "Laser speckle based digital optical methods in structural mechanics: A review," *Opt. Lasers Eng.*, vol. 87, pp. 32–58, Dec. 2016.
- [22] P. K. Rastogi, *Digital Speckle Pattern Interferometry and Related Techniques*. Chichester, U.K.: Wiley, 2001.
- [23] I. Yamaguchi, "Speckle displacement and decorrelation in the diffraction and image fields for small object deformation," *Optica Acta, Int. J. Opt.*, vol. 28, no. 10, pp. 1359–1376, Oct. 1981.
- [24] J. Fraden, *Handbook of Modern Sensors: Physics, Designs, and Applications*, 5th ed., Cham, Switzerland: Springer, 2016.
- [25] D. S. Bernstein, "Sensor performance specifications," *IEEE Control Syst. Mag.*, vol. 21, no. 4, pp. 9–18, Apr. 2001.
- [26] R. Leach, *Optical Measurement of Surface Topography*. Berlin, Germany: Springer, 2011.
- [27] D. Wertjanz, E. Csencsics, and G. Schitter, "An efficient control transition scheme between stabilization and tracking task of a MAGLEV platform enabling active vibration compensation," in *Proc. IEEE/ASME Int. Conf. Adv. Intell. Mechatronics (AIM)*, Jul. 2020, pp. 1943–1948.
- [28] E.-R. Olderog and H. Dierks, *Real-time Systems: Formal Specification and Automatic Verification*. Cambridge, U.K.: Cambridge Univ. Press, 2008.
- [29] S. Ito and G. Schitter, "Comparison and classification of high-precision actuators based on stiffness influencing vibration isolation," *IEEE/ASME Trans. Mechatronics*, vol. 21, no. 2, pp. 1169–1178, Apr. 2016.
- [30] E. Csencsics and G. Schitter, "Parametric PID controller tuning for a fast steering mirror," in *Proc. IEEE Conf. Control Technol. Appl. (CCTA)*, Aug. 2017, pp. 1673–1678.
- [31] W. K. Ho, C. C. Hang, and L. S. Cao, "Tuning of PID controllers based on gain and phase margin specifications," *Automatica*, vol. 31, no. 3, pp. 497–502, Mar. 1995.
- [32] K. J. Åström and T. Häggglund, *PID Controllers: Theory, Design, and Tuning*, 2nd ed., Research Triangle Park, NC, USA: Instrument Society of America, 1995.
- [33] M. Kamalidar, S. A. U. Islam, S. Sanjeevini, A. Goel, J. B. Hoagg, and D. S. Bernstein, "Adaptive digital PID control of first-order-lag-plus-dead-time dynamics with sensor, actuator, and feedback nonlinearities," *Adv. Control Appl.*, vol. 1, no. 1, p. 20, Dec. 2019.
- [34] R. Paris, T. Thurner, and G. Schitter, "Compensation based displacement measurement using objective laser speckles," *IFAC Proc. Volumes*, vol. 46, no. 5, pp. 264–270, 2013.
- [35] S. J. Kirkpatrick, D. D. Duncan, and E. M. Wells-Gray, "Detrimental effects of speckle-pixel size matching in laser speckle contrast imaging," *Opt. Lett.*, vol. 33, no. 24, pp. 2886–2888, Dec. 2008.
- [36] Y.-S. Jang and S.-W. Kim, "Compensation of the refractive index of air in laser interferometer for distance measurement: A review," *Int. J. Precis. Eng. Manuf.*, vol. 18, no. 12, pp. 1881–1890, Dec. 2017.
- [37] T. Fricke-Begemann, "Three-dimensional deformation field measurement with digital speckle correlation," *Appl. Opt.*, vol. 42, no. 34, pp. 6783–6796, Dec. 2003.
- [38] P. Bing, X. Hui-Min, X. Bo-Qin, and D. Fu-Long, "Performance of sub-pixel registration algorithms in digital image correlation," *Meas. Sci. Technol.*, vol. 17, no. 6, pp. 1615–1621, May 2006.
- [39] M. A. Sutton, J. H. Yan, V. Tiwari, H. W. Schreier, and J. J. Orteu, "The effect of out-of-plane motion on 2D and 3D digital image correlation measurements," *Opt. Lasers Eng.*, vol. 46, no. 10, pp. 746–757, Oct. 2008.
- [40] D. Wertjanz, E. Csencsics, T. Kern, and G. Schitter, "Bringing the lab to the fab: Robot-based inline measurement system for precise 3-D surface inspection in vibrational environments," *IEEE Trans. Ind. Electron.*, vol. 69, no. 10, pp. 10666–10673, Oct. 2022.
- [41] T. O. H. Charrett, Y. K. Bandari, F. Michel, J. Ding, S. W. Williams, and R. P. Tatam, "A non-contact laser speckle sensor for the measurement of robotic tool speed," *Robot. Comput.-Integr. Manuf.*, vol. 53, pp. 187–196, Oct. 2018.
- [42] Z. Ge, Y. Gao, H. K.-H. So, and E. Y. Lam, "Event-based laser speckle correlation for micro motion estimation," *Opt. Lett.*, vol. 46, no. 16, pp. 3885–3888, Aug. 2021.



Matthias Laimer received the M.Sc. degree in electrical engineering from TU Wien, Vienna, Austria, in 2022.

He is currently a Doctoral Researcher with the Automation and Control Institute (ACIN), TU Wien. His primary research interests are on industrial automation and robot-based inline measurement systems.



Thomas Kern (Graduate Student Member, IEEE) received the M.Sc. degree in electrical engineering from TU Wien, Vienna, Austria, in 2024.

He is currently a Doctoral Researcher with the Automation and Control Institute (ACIN), TU Wien. His primary research interests are on optical inline measurement systems and precision measurements in motion.



Lara Brukner received the B.Sc. degree in technical physics from TU Wien, Vienna, Austria, in 2022.

She is a Student Assistant with the Automation and Control Institute (ACIN), TU Wien. Her primary research interests are on optical displacement measurements.



Georg Schitter (Senior Member, IEEE) received the M.Sc. degree in electrical engineering from TU Graz, Graz, Austria, in 2000, and the M.Sc. and Ph.D. degrees from ETH Zurich, Zürich, Switzerland, in 2004.

He is currently a Professor of advanced mechatronic systems with the Automation and Control Institute (ACIN), TU Wien, Vienna, Austria. His primary research interests are on high-performance mechatronic systems, particularly for applications in the high-tech industry, scientific instrumentation, and mechatronic imaging systems, such as AFM, scanning laser and LIDAR systems, telescope systems, adaptive optics, and lithography systems for semiconductor industry.

Dr. Schitter received the journal Best Paper Award of IEEE/ASME TRANSACTIONS ON MECHATRONICS in 2018, the IFAC Mechatronics from 2008 to 2010, the Asian Journal of Control from 2004 to 2005, and the 2013 IFAC Mechatronics Young Researcher Award. He served as an Associate Editor for *IFAC Mechatronics*, *Control Engineering Practice*, and IEEE TRANSACTIONS ON MECHATRONICS.



Ernst Csencsics (Member, IEEE) received the M.Sc. and Ph.D. degrees (Hons.) in electrical engineering from TU Wien, Vienna, Austria, in 2014 and 2017, respectively.

He is currently an Associate Professor of measurement systems with the Automation and Control Institute (ACIN), TU Wien. His primary research interests are on opto-mechatronic measurement and imaging systems, high-performance mechatronics, scientific instrumentation, precision engineering, and advanced robotic inline measurement systems.

Dr. Csencsics received the Journal Best Paper Award of IEEE/ASME TRANSACTIONS ON MECHATRONICS in 2018, the Best Paper Award at the IEEE International Instrumentation and Measurement Technology Conference in 2022, and the Best Student Paper Award at the American Control Conference in 2016.